8

Ultrasonic Thruster

Alfred C. H. Tan and Franz S. Hover
Massachusetts Institute of Technology
United States of America

1. Introduction

Acoustic streaming refers to the bulk net flow of fluid generated as a result of intense, free-field ultrasound. This phenomenon, also known as 'quartz wind' or 'sonic wind', is induced by a loss in mean momentum flux due to sound absorption in the fluid medium, leading to a net flow along the transducer axial direction. The transmission of intense sound energy into the fluid is also associated with a resultant force acting on the transducer surface. This resultant "backthrust" can be exploited in underwater vehicles for propulsion or maneuvering purposes. We refer to the device as ultrasonic thruster (UST), shown in Fig. 1, and define it as an ultrasonic transducer made from piezoelectric material, excited by an alternating high-voltage source in the megahertz. We provide a general comparison between various propulsion technologies in Table 1.

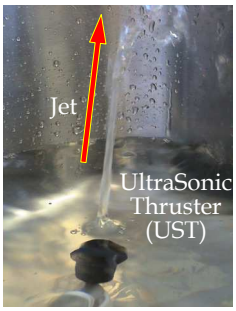

Fig. 1. An ultrasonic thrusters (UST) directing a jet through the free water surface.

The UST we describe is being considered as an alternative small-scale propulsor for underwater robotic devices and systems, because it has no moving parts beyond its membrane and can be mounted flushed with the body of the watercraft. At a sound level of 132dB (re 1μPa) (Panchal, Takahashi, & Avery, 1995; Tan & Tanaka, 2006), it is destructive to biofouling and could perform self-cleaning under prolonged water submersion. These novelties in low maintenance and design robustness, coupled with low cost commercially off-the-shelf (COTS) transducers, are attributes which are not found in rotary or biomimetic propulsors of today. For a small transducer diameter of 1cm, thrust generated is in the order of tens of milli-newtons (mN), suitable for systems operating at low Reynolds numbers.

Propulsors	Advantages	Disadvantages
Fixed-pitch propeller	Very mature technology; cost effective	Load- and speed-dependent performance
Podded drive	Maneuverability; reduced impact on vessel internal layout; noise isolation	High bearing loads; costly and complex
Ducted propeller	High efficiency; directional stability; robustness against line fouling	May be inefficient at off design conditions
Controllable-pitch propeller	High efficiency at different advance speeds and loadings	Complex actuation system and maintenance
Waterjet	Efficient at high vessel speeds; suitable for shallow water	Poor performance at low speeds; vulnerable to ingested debris
Cycloidal propeller	Low-speed maneuverability	Complex mechanical structure and maintenance
Biomimetic – body/caudal fin (BCF) locomotion	Efficient and maneuverable at many speeds; quiet	Complex physical design
Biomimetic – Median and/or paired fin (MPF) locomotion	High maneuverability at low speeds; quiet	Complex physical design
Ultrasonic thruster (this work)	Very small size; no moving parts; short-range acoustic communication	Poor propulsive efficiency; requires a high-voltage supply

Table 1. Broad comparison of propulsor technologies (Carlton, 2007; Sfakiotakis, Lane, & Davies, 1999; Tan & Hover, 2009).

At the same time, large-scale collaborative swarm of small "microrobots" or "pods" systems are also gaining more interest in terms of low cost and practical operation. Small clusters of exploratory underwater vehicles could also acquire true flexibility in formation morphing, and wide spatial/temporal coverage in search-survey work (Trimmer & Jebens, 1989). More importantly, small water submersible is valuable in cluttered or confined environments such as inside a piping network or complex underwater structures (Egeskov, Bech, Bowley, & Aage, 1995). Naval reconnaissance missions could involve the deployment of clusters of expendable (even biodegradable) small underwater robots for hazardous/security missions such as mine-hunting or surveillance mapping (Doty et al., 1998).

In the following sections, we examine the theoretical background of the UST thrust generation, introduce scaled parameters for comparison between various UST devices found in the literature, examine its transit efficiency, identify some thermal anomalies, and discuss some of the UST design considerations. A detailed construction of the UST will be outlined with underlying insights to materials selection and design principles. For practical demonstration, we have also built a small underwater vehicle named *Huygens*, to establish a miniaturized platform for supporting multi-objectives subsea tasks. The main focus will be exclusively on the transducer-only testing (without nozzle appendages) for thrust and wake characterization as these are fundamentals toward understanding the UST technology. Prior

works on thrust by ultrasonic means can be found in (Allison, Springer, & Van Dam, 2008; Nobunaga, 2004; Wang et al., 2011; Yu & Kim, 2004); we review and expand upon these. We have also made a comparison among these UST technologies, and provide some insights into some of the design parameters of ultrasonic propulsion.

2. Underwater Ultrasonic Thruster (UST)

The UST is made from a membrane actuator mounted in a specially designed waterproof housing, excited by an electrical source at ultrasonic frequency; the UST is generally applied underwater to generate thrust. For this work, the actuator is made of a thin, circular piezoelectric plate. We establish some fundamental concepts of the UST physics leading to thrust as experienced on the transducer surface, and its resulting jet of acoustic streaming into the farfield. Several nomenclatures are defined and used to describe the experimental results in the preceding sections.

2.1 Thrust generation

As described in the introduction, there are some prior works on the UST found in the literature. The experimental model used in those examples varies in shapes and sizes, and in the following, we provide a basis of comparison among them in terms of thrust density and electrical power density between each UST design. As an introduction, we refer to the mathematical treatment of thrust and acoustic power generation in Eqs. (1) to (4) as originally proposed by (Allison, et al., 2008), and relates thrust to the transducer voltage supplied, *E*, a parameter reported in most UST-related studies.

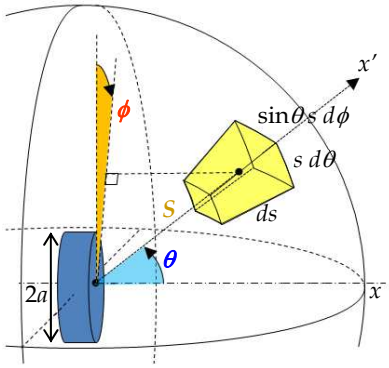

Fig. 2. An elemental control volume in the far-field; the elevation angle, azimuth angle and distance from the center of transducer are θ, ϕ, and s respectively.

In Fig. 2, several variables for the transducer and the acoustic field are introduced. The acoustic energy transmits to the right semi-hemisphere, propagating perpendicularly through an elemental cross-sectional surface area $dS = s^2 \sin\theta d\theta d\phi$ of a control volume $dS = s^2 \sin\theta d\theta d\phi ds$. According to (Allison, et al., 2008), thrust experienced on the surface of the transducer is expressed as

$$T = \rho \upsilon_o^2 a^2 \pi \int_0^{\theta_1} \frac{J_1(ka\sin\theta)^2}{\sin\theta} d\theta \tag{1}$$

where ρ (kg/m^3), υ_o (m/s), a (m), k, β, and $J_1(\cdot)$ denote the fluid density, transducer surface velocity, radius of the transducer, wavenumber, sound absorption coefficient, and Bessel function of the first kind, respectively, and we consider $\theta_1 = \sin^{-1}\frac{3.832}{ka}$ (Blackstock, 2000) as the upper limit of the dominant ultrasonic beamwidth.

The relationship between the acoustic power along the transducer axial direction x and the ultrasonic thrust is given by a simple relationship (Allison, et al., 2008)

$$P_x = cT/\eta \tag{2}$$

where c (m/s) denotes the sound speed, and η relates to the efficiency which will be elaborated in the next paragraph. As we verify below, this also means the thrust is considerably lower than would a rotary propulsor operating at the same power level.

At s = 0, this acoustic power radiation is associated with the electrical power consumption across the transducer. The electrical power would provide an approximation to the acoustic power loading, which relates to the thrust force, and is reflected in the following considerations through an efficiency constant, η; (i) electrical power lost across the transducer is not wholly transferred into the medium; (ii) acoustic loading at the sharp dominant resonant frequency of the transducer may not be precisely tuned; (iii) it is difficult to consider the equivalent acoustic load in the lumped circuit impedance; (iv) although the acoustic power is mainly generated within the narrow ultrasonic beam, some losses also occur outside the beamwidth.

By relating the thrust production to the root mean square of the transducer voltage supplied, E_{rms}, it can be equated as

$$T = \frac{\eta E_{rms}^2}{c\,\mathrm{Re}(\Re)} \tag{3}$$

where Re($\Re$) is the real component of the transducer impedance, and the electrical power,

$$P = \frac{E_{rms}^2}{\mathrm{Re}(\Re)} \tag{4}$$

corresponds to P_x at s = 0. This thrust scaling with squared voltage in (3) will be used in Section 2.3.4.

2.2 Acoustic streaming

Following Lighthill (Lighthill, 1978), acoustic streaming arises because of acoustic energy absorption along the path of propagation in a viscous, dissipative fluid medium. A simple explanation of the mechanism can be thought of as exit momentum flux from each exposed

fluid particle is less than it entered due to sound absorption. The distribution of energy gradient then moves the particle away from the source resulting in an overall streaming effect. In another words, the loss in momentum flux across a control volume (Fig. 2) leads to a net force in the direction of the acoustic path. This net force in turn generates hydrodynamic flow in a steady state incompressible medium, as governed by the Navier-Stokes equation,

$$\rho \overline{u}_x \frac{\partial \overline{u}_x}{\partial x} = -\frac{\partial \overline{p}_0}{\partial x} + \mu \frac{\partial^2 \overline{u}_x}{\partial x^2} + F_x \tag{5}$$

where $\overline{u}_x$ denotes the time-averaged streaming velocity along the x-axis, F_x is the radiation force along the x-axis, p_0 is defined as $p_0 = \rho c \upsilon_0$, and μ (kg/m·s) is the dynamic viscosity of the fluid. Since mass flow is conserved within the control volume, that is, $\rho \frac{\partial \overline{u}_x}{\partial x} = 0$, Eq. (5) can be solved by assuming $F_x = A e^{-\beta x}$ and using boundary conditions $\overline{u}_x(0) = 0$, $\overline{u}_x(\infty) = 0$, to obtain

$$\overline{u}_x = \frac{A}{\nu\left(B^2 - \beta^2\right)}\left[e^{-\beta x} - e^{-Bx}\right] \tag{6}$$

where A and B are characteristic coefficients of the fully developed axial velocity profile ($t \to \infty$), and ν is the kinematic viscosity $\nu = \mu/\rho$ (m²/s), $\beta = 2\alpha$ for low intensity sound, and α (dB/m) is the absorption coefficient at a particular sound transmission frequency (Rudenko & Soluian, 1977). Accordingly, Lighthill demonstrated that the radiation force can also be represented by the Reynolds stress along the axial direction:

$$\overline{F}' = -\frac{\partial \rho \overline{u}_x^2}{\partial x} \tag{7}$$

In this case, it follows from Eq. (7) that $\overline{F}'$ is proportional to $\overline{u}_x^2$ and knowing that $\overline{F}'$ is also proportional to E^2, $\overline{u}_x$ is seen to scale directly with E.

Next, the total fluid discharge across the lateral section of the flow in Fig. 3 is given by $u_r \delta A = u_r 2\pi r \delta r$ (Fig. 4), and the mass flow rate through the elemental disc is $\rho u_r 2\pi r dr$. From (Tan & Hover, 2009) and later in Section 2.3.4, it can be seen that the streaming field across a lateral section can be approximated by a Gaussian distribution of the following form, $u_r = u_x e^{-\frac{r^2}{2C^2}}$, where u_x (m/s) is the axial velocity in unit time, r (m) is the radial distance and C is a constant associated with the standard deviation of the Gaussian distribution. u_x reveals a vital difference from conventional propeller design and biomimetic actuation – that at $x = 0$, the streaming velocity at the surface of the transducer is zero. This observation is further verified in the experimental results in Section 2.3.4. Hence the total kinetic energy of the velocity field in unit time from $x = 0$ to $x = x_f$, where x_f (m) is the focal distance from the flat transducer surface, is given by

$$K.E. = \int_0^{x_f} \int_0^R \rho u_x u_r 2\pi r \, dr dx$$
$$= 2\pi\rho \int_0^{x_f} \int_0^R u_x^2 r e^{-\frac{r^2}{2C^2}} dr dx \tag{8}$$

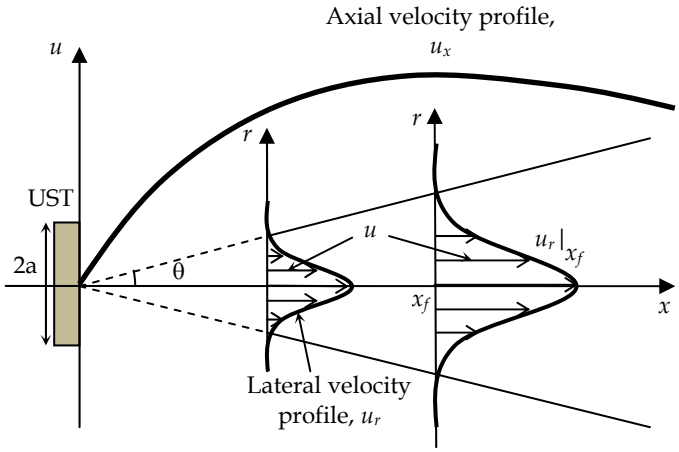

Fig. 3. Velocity distribution of the acoustic streaming. Lateral velocity profile approximates a Gaussian distribution while axial velocity follows a rapid increase in velocity before a gradual decline.

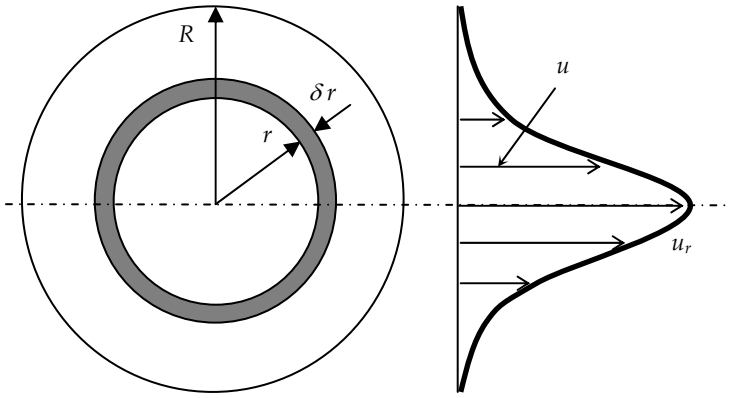

Fig. 4. An elemental disc sectioned laterally from the ultrasonic field. Axis of the transducer passes through the center of the concentric circles. The shaded annulus area, $2\pi r \delta r$, is an elemental area through which flow discharges.

where R (m) is the radius of u_r (m/s) profile subtended by θ_1 at x_f, and the overbar is omitted for simplicity. Substituting Eq. (6) into Eq. (8), and solving the double integral, the total kinetic energy in unit time becomes

$$K.E. = \frac{\pi\rho A^2 C^2}{\nu^2\left(B^2-\beta^2\right)^2}\left(-\frac{1}{\beta}e^{-2\beta x_f}+\frac{1}{\beta+B}e^{-(\beta+B)x_f}-\right.$$
$$\left.\frac{1}{B}e^{-2Bx_f}+\frac{1}{\beta}-\frac{1}{\beta+B}+\frac{1}{B}\right)\times\left(1-e^{-\frac{R^2}{2C^2}}\right) \quad (9)$$

While Eq. (9) sums up the total kinetic energy within the streaming field up to the focal distance, streaming at distances above x_f will evidently slow down, and free turbulence occurs due to the boundary between the stationary ambient water and the insonified flow – a process called entrainment. We consider regime $x > x_f$ to be no longer reliable or valid for *K.E.* calculation. Eq. (9) will be used in Section 2.3.4. Finally, it follows earlier that u_x scales directly with *E* and knowing that *K.E.* is also proportional to u_x^2 from Eq. (8), *K.E.* is seen to scale directly with E^2. This scaling of *K.E.* with square voltage will be used in Section 2.3.4 to determine the streaming energy and a comparison is made across other UST devices.

2.3 Thrust and wake experimental setup

In this section, we characterize thrust and wake energy for a specific UST design, and then investigate and how these properties can be modified using various source voltages. An underwater vehicle prototype was also constructed to demonstrate the ultrasonic propulsion capability.

2.3.1 UST hardware and methods

We use standard piezoelectric transducer technology for the conversion of electrical to acoustical energy. The transducer (Murata Manufacturing Co. Ltd) is made from a circular PZT plate measuring 7mm in diameter, housed in a 10mm diameter waterproof metallic casing as shown in Fig. 5.

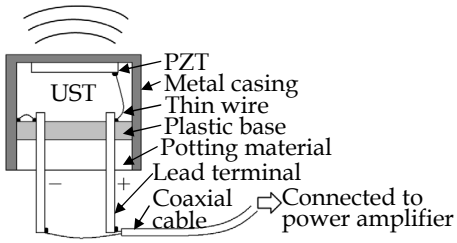

Fig. 5. Construction of the UST (adapted from Murata Manufacturing Co. Ltd).

In our prototype vehicle described below, three USTs are connected to switches for actuation control, and 50Ω coaxial cables connect the three switches to a single power amplifier (ENI 3100L). The ENI unit accepts an oscillatory input up to a maximum of $1V_{rms}$, and amplifies the output voltage by a gain of 50dB for a 50Ω output impedance. It is a Class A amplifier which means it will be unconditionally stable, and maintains linearity even with a combination of mismatched source and load impedance. When the ultrasonic transducer

emits intense acoustic energy into the fluid, the thin metal housing provides excellent heat dissipation. Natural convection and acoustic streaming also aid in carrying away heat from the transducer surface (Tan & Hover, 2010a).

2.3.2 Thrust force measurement

It is important to develop a reliable underwater thrust measurement method, especially for small thrust magnitudes as is the case of the UST. Most load cells are either non-submersible or could not provide sufficient sensitivity/resolution required at small driving forces. While thrust can also be inferred from acoustic intensity measurement using a hydrophone, it poses some challenges unique to the UST setup, such as membrane cavitation, heating effect, and reading errors averaged from a finite-size hydrophone. Indeed, (Hariharan et al., 2008) reported that acoustic intensity measurements do not perform well, having an error in excess of 20% with experimental data.

In order to accurately measure the thrust produced by the UST, we developed an approach which allows sensitivity control by sliding the UST along an L-shaped arm. Moment is measured with a high precision torque sensor. Other methods have been proposed for measuring these very fine-scale forces, for example, to attach and submerge a UST on one end of a vertical pendulum, hinged off-center, with the other end flexing a strain gauge (Allison, et al., 2008). Another approach is to attach the UST to a free-hanging wire and take photographs of the displacement as the UST is being actuated (Wang, et al., 2011; Yu & Kim, 2004). We found that the setup in Fig. 6 provides very good accuracy and repeatability, as indicated in the calibration plot of Fig. 7. The torque meter accuracy provided by the manufacturer is ±0.09mN·m, and the absolute error in the calibration thrust force averages about ±0.6mN, when our dial gauge is positioned 0.5m from the torque axis on the L-arm.

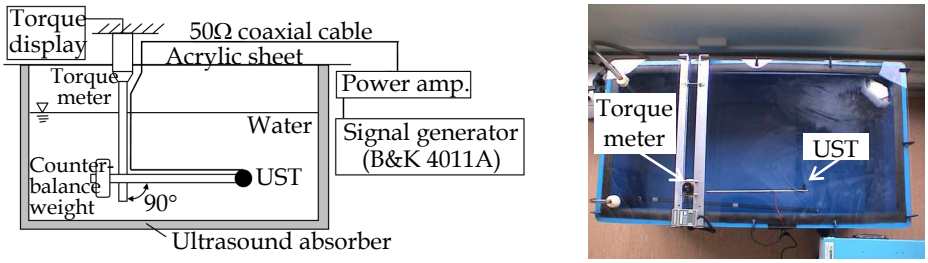

Fig. 6. (a) The semi-anechoic water tank and torque sensor used to measure UST thrust; thrust is generated in the direction perpendicular to the page. (b) A plan view of the UST thrust measurement setup.

Hence the total force uncertainty is around 0.8mN. Torque calibration is performed prior to all test sets. Thrust stabilizes and is recorded about ten seconds after turning on the power; then the power is turned off. We maintain a minimum of ten-second rest period between all tests, to allow for cooling and for the water to settle. The UST together with the L-shaped arm is submerged in an ultrasound semi-anechoic tank measuring 1.2m×0.6m×0.6m, filled with distilled water and covered with an acrylic sheet.

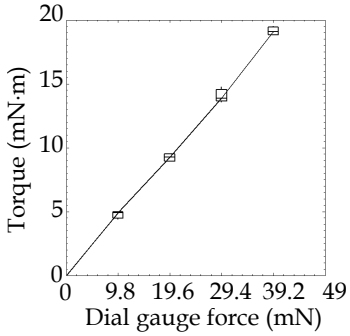

Fig. 7. Calibration of the test rig. Each of the four points shown is an average of four separate force applications using a sensitive dial gauge.

2.3.3 Acoustic streaming measurement

A 2-dimensional Digital Particle Image Velocimetry (DPIV) provides an accurate depiction of the UST wake, and beyond the entrainment boundary in the far-field. In similarly-scaled conditions, it has been reported that a 2% standard deviation at the point of maximum velocity can be expected with DPIV (Myers, Hariharan, & Banerjee, 2008). The DPIV system is set up in a water tank measuring 2.4m×0.7m×0.7m, as shown in Fig. 8. Calculated particle velocities are subject to noise depending predominantly on the interrogation window size, the number of seeded particles, and the sampling rate. We made efforts to tune these for the lowest noise level.

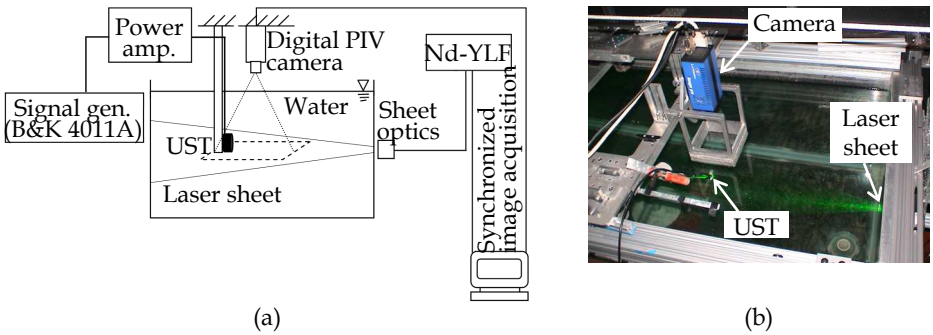

Fig. 8. (a) Schematic diagram of the DPIV tank setup. Acoustic streaming is illuminated by a laser sheet, and images are captured by a digital camera for post-processing. (b) A top view of the UST wake measurement setup.

A pulsed laser sheet, produced by a Quantronix diode pumped Q-switched frequency laser (Darwin-527-30M) and spreads horizontally through the water tank from the outside, coincident with the UST axis. The tank is seeded with 50μm polyamide particles, and a camera viewing the laser sheet perpendicularly traces the streaming particles when the UST is operating. The camera samples 300 timed, paired images at 400Hz, in a 0.2m×0.2m field of

view. Post-processing is carried out using DaVis 7.1 software. The UST transducer is positioned at 1.2m from the sheet optics, 0.4m from each adjacent tank wall, and 0.3m below the water surface. The time taken for the stream to become established has been reported variously at about 0.5s (Loh & Lee, 2004) and 20s (Kamakura, Sudo, Matsuda, & Kumamoto, 1996). We allow at least one minute of flow before the camera starts recording. Specific kinetic energy of the flow up to the focal distance x_f is shown in the next section, which averages 150 measurements; recording the frames takes less than one second. Then the power is turned off, and the tank water is allowed to settle for at least one minute. This schedule is not the same for thrust measurements, as the transducer is powered and cooled for a considerably longer time during DPIV tests. A more detailed analysis of the transducer heating is presented in Section 3.

2.3.4 Thrust and streaming results

Fig. 9(a) shows thrust force as a function of frequency, for a sinusoidal waveform. The thrust has obvious peaks near 11mN when operated at 7MHz, which can also be computed using the thickness mode frequency constant, $N_t = f_0 h$, where h (m) is the thickness of the PZT, and $N_t = 1970$ as specified by the manufacturer. We will focus on this frequency in most of the discussion to follow. Fig. 9(b) illustrates the DPIV velocity field for a sinusoidal waveform at 7MHz, with amplified output voltage $54V_{rms}$. From Fig. 10(a) and 10(b), the maximum axial streaming velocity is observed at the point (0mm, 120mm) in the DPIV image, illustrating a fundamental feature of the UST – *that net fluid flow is zero at the transducer face*. Considering the same waveform configurations and frequencies as in Fig. 9(a), a similar peak at 7MHz in the total kinetic energy can be seen in Fig. 9(b).

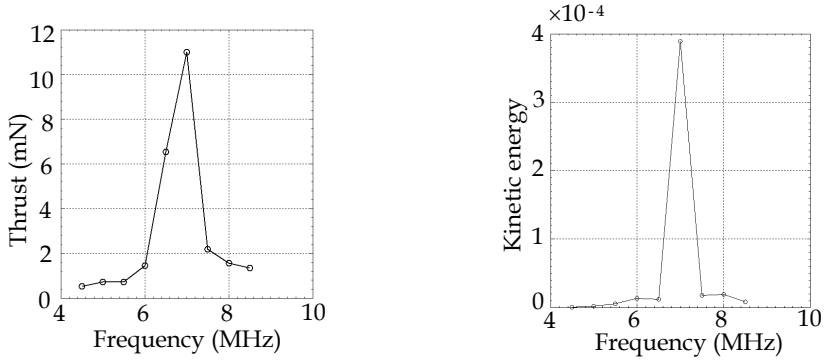

Fig. 9. (a) Measured thrust versus source frequency for sinusoidal waveforms supplied at $59V_{rms}$. (b) Total kinetic energy versus source frequency, from DPIV. The sinusoidal signal is supplied at $54V_{rms}$.

Figs. 11(a) and 11(b) summarize our findings specifically at the 7MHz resonant point. Thrust generally increases with output voltage, but then starts to flatten out above the amplified output voltage of $60V_{rms}$. From Fig. 12 and from Eq. (3), the corresponding scaled thrust level is $3.8\times10^{-3}mN/V^2$ at $59V_{rms}$. Scaled thrust decreases gradually as the output voltage increases, and the absolute thrust appears to saturate above $60V_{rms}$; see Fig. 12 – a result also

reported in another publication (Tan & Hover, 2010a). The kinetic energy data in Fig. 9(b) show similar trend as well. Using the *K.E.*-E^2 proportionality relationship from Section 2.2, the scaled kinetic energy at $54V_{rms}$ is calculated to be $1.5\times10^{-7}W/V^2$ respectively. Both scaling of thrust and *K.E.* is important when we compare various UST devices later in Section 2.5.

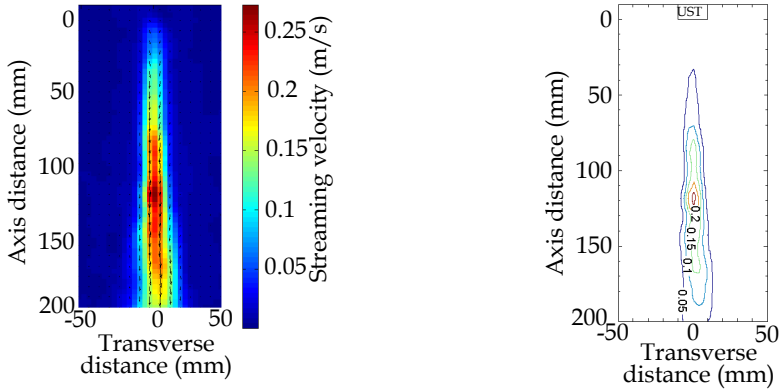

Fig. 10. (a) Digital Particle Image Velocimetry (DPIV) image of a jet at 7MHz, $54V_{rms}$. (b) Processed DPIV velocity field with each velocity contour step at 0.05m/s interval. A focal point can be clearly seen at (0mm, 120mm).

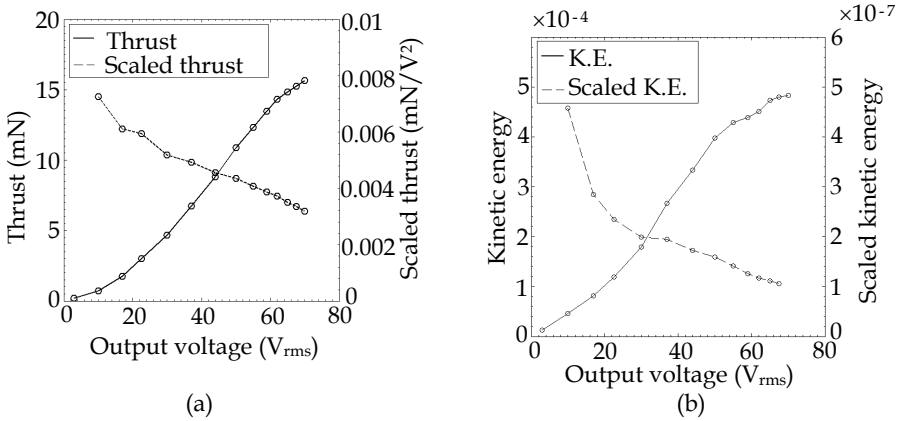

Fig. 11. (a) Measured thrust versus input voltage to the power amplifier using a 7MHz sinusoidal signal. Data appear to saturate above $60V_{rms}$, which implies a disproportionate relationship. (b) Total kinetic energy versus output voltage of the power amplifier using a 7MHz sinusoidal signal. Data appear to saturate above $55V_{rms}$, which also implies a disproportionate relationship.

Although increasing the output voltage always increases thrust, the wake velocity of the sinusoidal source appears to saturate near $55V_{rms}$. The phenomenon of saturation can be

explained by distortion in finite-amplitude traveling waves, according to weak shock theory. On the other hand, the fact that thrust in this case increases with input power despite the saturation of velocity highlights an unusual observation – that thrust production mechanism involves the wake only indirectly, and in a manner that is distinct from other propulsors. This fact may offer some interesting avenues for UST design, where the wake and the thrust force could be manipulated independently. This is especially useful in a scenario where larger thrust is desired but the wake has to be weak at the same time, for example, to minimize stirring up particulates near the seabed.

In summary, increasing the output voltage of the power amplifier will no doubt increase the thrust and kinetic energy production of the transducer, but at the same time, introduces an undesirable disproportionate relationship (Tan & Hover, 2010a). This will be further discussed in Section 3.

2.4 Small underwater vehicle, *Huygens*

We designed and constructed a small, streamlined shell with three embedded UST devices for propulsion and steering in the horizontal plane. The shell measures 215mm×160mm×80mm, profiled by a truncated NACA 0054 airfoil in the side view, and a truncated NACA 0025 airfoil in the plan view, as shown in Fig. 12(a). The shell is made from high-strength urethane foam for buoyancy, and coated with polyurethane. A UST is positioned at the rear end of the craft to provide forward thrust, and two USTs subtending 120° are symmetrically located on each side of the front end – at the "fish eyes" position. Together, these provide the right/left steering and backing thrust. Inside the shell, two rectangular cavities are machined, measuring 100mm×100mm×35mm, and 45mm×60mm×30mm. The shell can be opened into two halves via a stepped mid-section opening, lined with double O-rings for a watertight seal. The cylindrical UST seats are also lined with O-rings. The vent shown in the top left corner of Fig. 12(b) allows for a tether or an antenna for shallow-water wireless control.

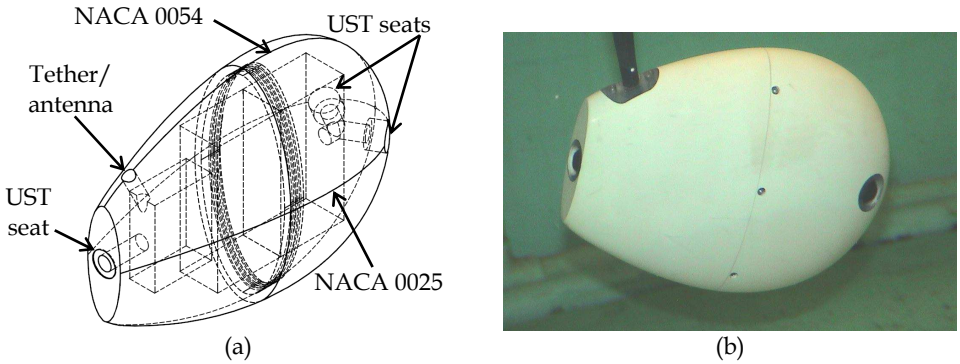

Fig. 12. (a) 3-D wire mesh view of *Huygens*. (b) A side view of *Huygens* prototype. Three transducers are installed on the shell with two at the frontal "eyes" positioned for steering and another in the rear for forward thrust. Tethered signal generates a multiplexed 7MHz sinusoidal input to the three USTs.

2.5 Ultrasonic propulsion design considerations

To our knowledge, there are only three experimental works on ultrasonic propulsors reported from (Allison, et al., 2008), (Yu & Kim, 2004), and (Wang, et al., 2011); we compare them with our UST in terms of thrust density, scaled thrust density and power density, in Table 2. As our UST system was operating at a resonance frequency and high voltage, it is difficult to make a fair and direct comparison of performance. We have employed a much higher power level, resulting in a very high thrust level and higher scaled thrust density.

Properties	Allison et al. (Allison, et al., 2008)	Yu et al. (Yu & Kim, 2004)	Z. Wang et al. (Wang, et al., 2011)	This work
Frequency (MHz)	5.5	10.8	17.8	7.0
Voltage (V)	24.5	46	140	59
Electrical power (W)	5	--	--	69.5
Transducer surface area (mm^2)	$\pi/4\times10^2$	5×5	$\pi/2\times1.28^2$	$\pi/4\times7^2$
Thrust (mN)	2.25	5.6	2.3	13.5
Thrust density (N/m^2)	28.6	224	893.7	350
Scaled thrust density ($N/m^2{\cdot}V^2$)	0.05	0.11	0.04	0.10
Electrical power density (kW/m^2)	64	--	--	1806

Table 2. Performance of different UST devices.

This latter property is important in applications because it indicates a very compact force source operating with reasonable voltage levels, exploitable to benefit from many of its unique ultrasonic attributes we discussed earlier in the introduction.

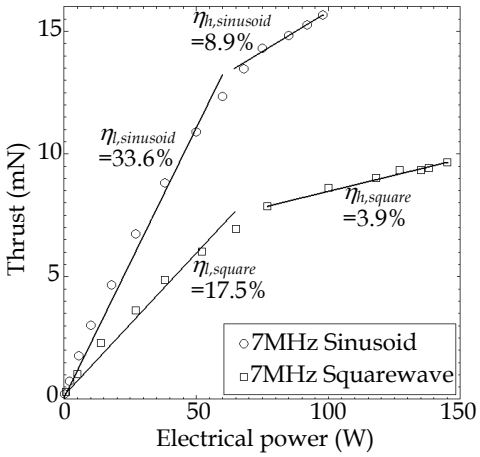

Fig. 13. Thrust force produced by the UST versus driving electrical power. The *l* and *h* subscripts indicate evident low- and high-power regimes. The output voltage to the sinusoid is $59V_{rms}$, and for the square wave is $54V_{rms}$.

Fig. 13 details the acoustic efficiency of the UST transmitting at a sinusoidal 7MHz. From Eq. (2), $T = \eta P/c$, where c is known (1480m/s), and T and P are measured. It can be made out that the sinusoidal waveform has two regimes relating thrust to electrical power – one of lower power with proportionally increasing thrust, and another somewhat saturated thrust at higher power. Below 70W electrical power, the power-thrust curve for sinusoidal input shows an acoustic efficiency of about 34%. Above 70W, the UST efficiency falls to less than 10%. Efficiency is calculated incrementally for each of the lines, that is, using the change in thrust versus the change in power. A square waveform is added in Fig. 13 for the sake of comparison. In general, the sinusoidal excitation is much more efficient than the square waveform. We note that the efficiency numbers given in (Allison, et al., 2008) are somewhat higher than what we show here, in part because of their custom transducer design, but also because they operated at much lower power levels. Below 2mN, we also achieve high efficiency around 70%. In respect to improving acoustic efficiency, other features such as nozzle appendages, shaping of UST, stacked piezoelectric layers could be considered.

2.5.1 Vehicle mission

In this subsection, we infer the expected speed and mission length that could reasonably be achieved from a UST-propelled underwater vehicle similar to *Huygens*. For our vehicle speed measurements, we used a high resolution Vision Research digital camera (Phantom V10) mounted with a wide-angle 20mm lens from Sigma. We sampled the advance speed of *Huygens* at 40samples/second over a straight course of 0.6m; the craft was allowed to accelerate for ten seconds before beginning the velocity measurement. Although a tether was attached to the vehicle for these tests, we maintained a large loop hanging below the vehicle, and moved the top of the tether along with the vehicle, using a sliding car and guiding post. With the recorded images of *Huygens*, the advance speed measured is a constant 0.049m/s.

The vehicle is quite streamlined, with only small holes around the frontal USTs, and a flat trim at the rear. From the top sectional view of *Huygens*, we can approximate the overall profile as an airfoil with a thickness-to-chord ratio of 0.37, and a span of 0.16m. The Reynolds number is $\mathrm{Re} = \dfrac{\rho U l_c}{\mu}$, where ρ (kg/m^3), U (m/s), l_c (m) and μ (kg/m·s) denote the fluid density, advance speed of the vehicle, chord length of the vehicle, and dynamic viscosity of the fluid respectively. The drag coefficient is $C_d = \dfrac{2T}{\rho A_w U^2}$, where T (N) and A_w (m^3) denote the thrust force, and wetted surface area respectively. Expressing U on the left hand side of Re and C_d separately, the Reynolds number and drag coefficient is related by

$$\mathrm{Re}^2 C_d = \frac{2\rho l_c^2 T}{A_w \mu^2}. \tag{10}$$

Using the Moody chart for a streamlined strut (Hoerner, 1965), U can then be estimated. To obtain the thrust, we recall that a sinusoidal input at 7MHz and 59V$_{\mathrm{rms}}$, creates a thrust force of T = 13.5mN (Fig. 11(a)). The constants ρ, l_c, A_w, and μ are 1000kg/m^3, 0.215m, 0.053m^2,

and 1.002×10^{-3}kg/m·s respectively. The parameter $\mathrm{Re}^2 C_d$, solved using Eq. (10), is 23.4×10^6, and for *Huygens*, a unique point can be identified on the $C_d - \mathrm{Re}$ Moody diagram; Re = 1.17×10^4 and $C_d = 0.17$. It is thus estimated that *Huygens* will advance at a velocity of 0.054m/s – very close to the observed value.

Regarding mission duration and length, a small 11V, 0.75Ah lithium-ion battery would occupy about 10% of the *Huygens* vehicle volume. We assume an average power capacity reduction of 90% in a single discharge cycle, providing about 7.4Wh of energy. The UST consumes 69W of electrical power with an acoustic efficiency of 33.6% (Fig. 13), to produce 13.5mN of thrust with a constant vehicle advance velocity of about 0.05m/s. If we assume the instrumentation and other loads are small compared to the propulsive load, a simple straight-path mission will last around six minutes and travel a distance of about twenty meters. A somewhat larger battery could power the vehicle for perhaps thirty minutes, with a mission length of one hundred meters. While the UST is clearly not competitive with rotary or some biomimetic propulsors in terms of transit efficiency, nonetheless these estimates show that maneuvering a very small-scale vehicle utilizing USTs offers a propulsive force with interesting thrust and wake characteristics.

(a)

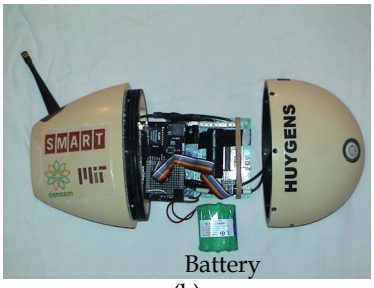

(b)

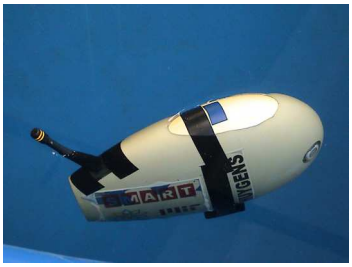

(c)

Fig. 14. (a) A specialized UST constructed from a one centimeter diameter piezoelectric transducer for underwater operation. (b) An internal view of the components of the wireless underwater vehicle, *Huygens*. (c) Wireless testing of *Huygens* in a laboratory tank.

We have also demonstrated a wireless version of *Huygens* (Fig. 14(c)) powered by a small on board battery (Fig. 14(b)). However, the electronics board could only supply limited power to each UST, and was able to slowly move the vehicle but inadequate to overcome the

vehicle drag very well. One solution could be to improve the UST power output through a small size ultrasound amplifier such as reported in (Lewis & Olbricht, 2008). We continue to make improvements to optimize the output thrust density with considerations to on board space budget, using specially constructed underwater UST (Fig. 14(a)), and higher energy density batteries as well.

3. Thermal dissipation of UST

As we observed in our previous work (Tan & Hover, 2009, 2010b), a disproportionate loss in thrust exist under elevated voltage applied across the transducer. As in all piezoelectric transducers, most of the electrical energy is converted into acoustical energy with some lost as superfluous heat through the transducer. In the presence of a large potential voltage, heat dissipation increases significantly, and dependent variables include the dielectric dissipation factor, transducer capacitance, and the presence of heat retardant materials next to the transducer. In instances of high power, localized heating at the soldered points may result in a failure or other undesirable outcome (Zhou & Rogers, 1995).

While temperature studies on PZT have been adequately described and investigated in the literature (Duck, Starritt, ter Haar, & Lunt, 1989; Sherrit et al., 2001), we are not aware of any work that makes a direct connection between transducer temperature rise and the propulsive thrust generated. As the UST is an underwater propulsor, knowledge of the conditions leading it to become a thermal source is important in many applications. In the following, we experimentally quantify the thermal distribution on the surface of the transducer under ultrasonic thrusting conditions, and introduce a dimensionless parameter to relate the thermal loss. In certain strategic applications, knowledge of this heat signature could aid in critical UST and system propulsion designs.

3.1 Heat transfer equations

We designed and constructed a larger UST unit based on (Allison, et al., 2008) but with several new features as shown in Fig. 15(a) and 15(b). Two o-rings are designed to seal the PZT against the water pressure and the air-backed layer provides maximum acoustic power transfer into the water. The screwed-on base holding the transducer is made of polytetrafluoroethylene (PTFE), so is the capping component holding the o-rings. Adhesive heat shrink and silicone potting seal the water from entering the air backing via the coaxial cable. The transducer material and medium will determine the heat transfer profile, rate of heat transfer and its dominant mode of heat transfer. For effective propulsion purpose, we add a layer of epoxy cast to match the acoustic impedance between the PZT and water.

From Fig. 16, in order to calculate the temperature profile through the transducer, $x = 0$ is taken at the centerline through the thickness of the PZT, and the average temperature at the centerline is given by

$$T_{mid} = \frac{Q_p x_p}{2 k_p A_p}\left(\frac{1}{\pi^2} + \frac{1}{4}\right) + T_p \tag{11}$$

where x_p (m) is the thickness of the transducer, k_p (W/m·°C) is the thermal conductivity of the transducer, A_p (m²) is the surface area of the transducer, and T_p (°C) is the temperature at

the interface between the transducer and epoxy layer (Sherrit, et al., 2001). Q_p (W) is the average heat transfer rate of the piezoelectric material, which is also the average power dissipation, given by

$$Q_p = 2\pi f C \tan\delta E_{rms}^2 \tag{12}$$

where f (Hz) is the resonance frequency, C (F) is the capacitance of the transducer, tan δ (%) is the dielectric dissipation factor, and E_{rms} (V_{rms}) is the root-mean-square of the applied voltage. It is important to understand that under high power and temperature conditions, the transducer's dielectric dissipation factor will change with the voltage applied, temperature and fluidic load. Consequently, the capacitance and dielectricity also vary nonlinearly as the voltage and temperature increase, incurring significant errors if these are not carefully characterized under elevated settings. The temperature profile of the piezoelectric material takes on a parabolic distribution, peaking at T_{mid} (°C), and either surface of the transducer has the same temperature, T_p; see Fig. 16. In addition, as we verify in Section 3.4 for the Biot number, we consider convection to be more important than the internal conduction which exhibits a nearly uniform temperature gradient within the homogenous solid body (PZT).

Fig. 15. (a) Sectioned view of the modular UST. A female Teflon cap is screwed onto the base holder which holds the transducer. O-rings provide the water-tight seals, and silicone potting provides flexibility and waterproofing to the coaxial cable connection. (b) An exploded view of the components of the modular UST.

The 1-dimensional Fourier's law is used to describe the thermal conduction of heat through the layer of epoxy cast on the UST water-side surface, and is governed by the heat flux, q (W/m^2), and the heat transfer rate (W) is given by

$$Q_e = qA_e = k_e A_e \frac{\left(T_p - T_e\right)}{x_e} \tag{13}$$

where k_e (W/m·°C) is the thermal conductivity, T_e (°C) is the surface temperature of the epoxy cast facing the water, and x_e (m) is the thickness of the epoxy cast. q is positive if heat flows along the positive x-direction, and vice versa.

As heat transfers into the water, convection will be dominant (heat radiation is negligible in our case) and using the steady-state Newton's Law of cooling, the convection governing equation is described as

$$Q_c = \bar{h} A_c \left(T_e - T_\infty \right) \tag{14}$$

where $\bar{h}$ is the averaged convective heat transfer (W/m^2·°C), A_c is the area of transducer exposed to the water (m^2), and T_∞ is the ambient water tank temperature (°C).

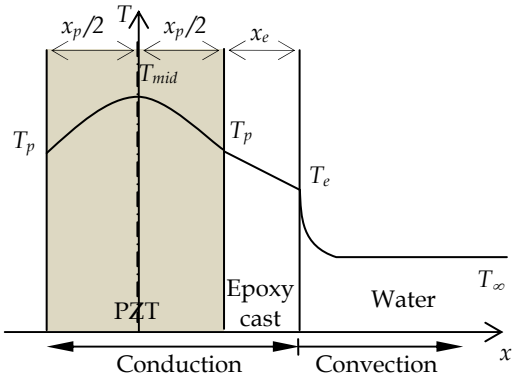

Fig. 16. A schematic diagram of the heat transfer profile. Acoustic transmission is generated by a transducer made from a PZT, through an epoxy cast layer into the water. Temperature gradient in each material outlines their relative heat transmission.

3.2 Temperature experimental setup

In this section, we characterize temperature for a 50mm UST transducer under increasing power, and then investigate in detail how various parameters could provide insights to the overall UST design consideration.

3.2.1 Hardware and methods

Fig. 17(a) shows the experimental setup similar to Fig. 6(a) except with an addition temperature data logger. Voltage to the amplifier is increased incrementally in steps of $0.2V_{pp}$ up to a maximum of $1V_{pp}$. The output power to the transducer depends on the transducer load capacitance and electrical impedance, and is not explicitly controlled.

The PZT (k_p = 1.25W/m·°C) measures 50mm in diameter and 2.1mm thick, and resonates at 1MHz. The epoxy cast layer (k_e = 0.22W/m·°C) is designed to be 0.6mm thick, with the same diameter as the transducer but the o-ring seals part of it, and only 42.2mm of the diameter is exposed to the water. The UST is vertically positioned with the surface facing the side wall of the 1.2m×0.6m×0.6m water tank, submerged at 0.2m from the bottom of the tank. Tap water is filled and stood for at least one day before the experiment begins, and ambient water temperature is regularly maintained at 21.5°C with sufficient cooling. Water is filled up to a depth of 0.45m.

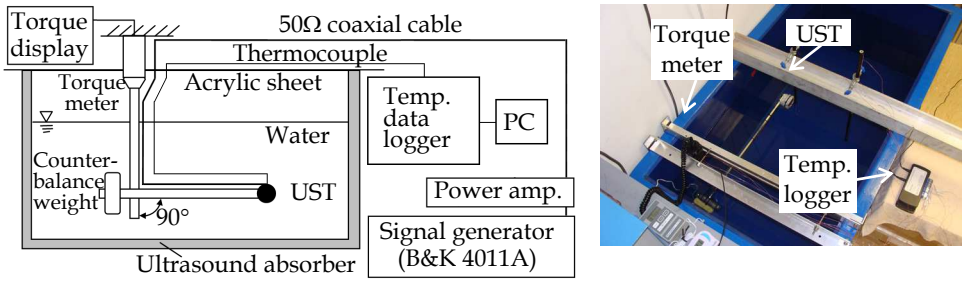

Fig. 17. (a) The experimental setup used to measure the UST temperature and thrust at the same time. Thrust is generated in the normal direction and out of the page. (b) A top view of the UST temperature measurement setup.

Similar torque calibration is performed prior to each set of test as discussed in Section 2.3.2. The sensing tip of five AWG 36 T-type (copper-constantan) thermocouples (SW-TTC2-F36-CL1) is attached to the transducer surface at five locations; T1 (north), T2 (east), T3 (west), T4 (south), and T5 (center) when viewed face-on as shown in Fig. 18. Thermal grease is applied to the junction of the thermocouples for improved thermal contact and each junction is affixed to the surface with a small adhesive tape. All thermocouples measure 2m in length and each terminates at a type-T miniature plug (CN001-T) is plugged into an Eight Channel Thermocouple Logger (OctTemp, MadgeTech), which has corrected cold-junction compensation internally for improved accuracy and response time. Each of the thermocouple is wrapped with an electromagnetic interference (EMI) tape and grounded to remove any RF interference. All temperature sensors have been calibrated by the manufacturer and are prescribed with an accuracy of ±0.5°C. Temperature data is sampled at 4Hz for all channels. The data logger has a background temperature noise of less than 0.1°C. Overall, temperature measurement uncertainty is estimated to be ±1°C in all cases. We consider a quasi-steady state of heat transfer to be defined by a temperature change of 0.2°C in a minute for 3 minutes.

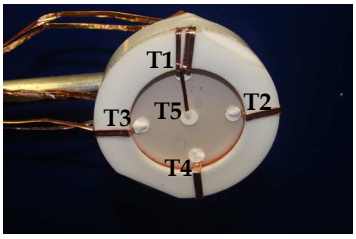

Fig. 18. Locations of thermocouples on the UST surface for average temperature measurement. Thermocouple cables are wrapped with RFI tape to ground RF interference.

3.3 Thermal characteristics results

Each temperature profile at a particular applied power is repeated four times independently under ambient water conditions. The experiment begins by recording 5 seconds of ambient

water temperature, after which the power amplifier is switched on for about 9mins. During this time, the transducer is observed to increase its temperature steadily and then stabilizes. 9mins into the actuation, all thermocouple achieve a quasi-steady state and the power amplifier is switched off. Cooling proceeds for another 10mins and the tank is allowed to settle. Ambient temperature of the water tank is monitored separately at the start and end of the experiment, and further cooling is allowed if the ambient water temperature increased significantly.

Generally, increasing the input voltage (in steps of $0.2V_{pp}$ to $1.0V_{pp}$) to the amplifier increases the temperature recorded on the transducer surface. Table 3 summarizes the input voltage to the amplifier, output voltage and output power of the amplifier, the corresponding thrust, and the mean transducer surface temperature. Four sets of data are each tabulated for the output voltage, output power, and thrust, to demonstrate the consistency of the system.

Using the output power and thrust columns of Table 3, a plot of thrust versus power is shown in Fig. 19. From Eq. (2), the acoustic efficiency of the UST can be worked out, which essentially is the gradient at each cluster of points multiply by the speed of sound in the water, *c*. Generally at lower power, the efficiency is higher, however, effective thrust is also lower, which may not be practically useful. As the power increases, efficiency declines rapidly and Fig. 19 illustrates the trend. In Fig. 19, it can be seen that generated thrust starts to decline at higher electrical power level. However, as we discuss below, the acoustic efficiency is observed to vary approximately in a first-order fashion as *P* increases. Ultrasonic thrust appears to begin to saturate near 16mN.

Input voltage (V_{pp})	Output voltage (V_{rms})	Output power (W)	Thrust (mN)	Mean surface temp. (°C)
0.2	13, 13, 12, 13	3.2, 3.2, 2.9, 3.2	4.59, 4.44, 4.59, 4.52	22.9
0.4	30, 29, 28, 29	18.0, 16.8, 15.6, 16.8	7.08, 7.01, 6.93, 6.86	26.7
0.6	48, 47, 47, 48	45.6, 43.6, 43.6, 45.6	10.85, 10.70, 10.70, 10.78	30.6
0.8	67, 66, 66, 67	90.4, 87.2, 87.2, 90.4	14.85, 14.77, 14.62, 14.85	35.0
1.0	86, 84, 86, 86	147.8, 141.8, 147.8, 147.8	16.43, 16.43, 16.5, 16.35, 16.5	39.2

Table 3. Table of output power from the amplifier and the corresponding thrust generated. Four sets of data from each stepped input voltage are recorded. Ambient tank temperature is maintained at 21.5°C.

3.3.1 Thermal losses at high voltage

To calculate the averaged convective heat transfer, we use the lumped-capacity solution for a heated body transferring heat into the water by free convection. The solution can be solved for T (t = 0) to give (Lienhard IV & Lienhard V, 2002)

$$T = \left(T_e - T_\infty\right) e^{-t/\tau} + T_\infty \tag{15}$$

where T (°C) is the time-variant temperature of the epoxy with respect to time t (s), T_e (°C) is the averaged temperature of the epoxy surface determined as [22.9, 26.7, 30.6, 35.0, 39.2]°C from the stepped input voltage, and T_∞ (°C) is the ambient tank temperature at 21.5°C. $\tau = \frac{\rho_e c_e V_e}{\bar{h} A_e}$ is the time constant of the cooling process, where ρ = 1200 kg/m^3 is the density of the epoxy, c_e = 1110 J/kg·°C is the specific heat capacity of epoxy, V_e = 8.4×10^{-7}m^3 is the volume of the epoxy through which sound transmits, $\bar{h}$ (W/m^2·°C) is the average convective heat transfer coefficient determined as [25, 24, 22, 18, 14]W/m^2·°C from the stepped input voltage, and A_e = 5.6×10^{-3}m^2 is the cross-sectional area of the epoxy through which sound transmits (note $A_e = A_p$).

Most of this transmitted heat energy is convected away into the water as the surface of the transducer heats up. With this knowledge and the acoustic efficiency plot in Fig. 19, where efficiency decline rapidly as output power increases, we can see that the supplied electrical power has been significantly converted into heat energy while thrust increased diminutively – that net thrust begins to saturate above 90W. In the region of the saturated thrust, we also note an increase in heating of the transducer when the power applied is increased further, explaining the fundamental cause of loss of thrust at high electrical power.

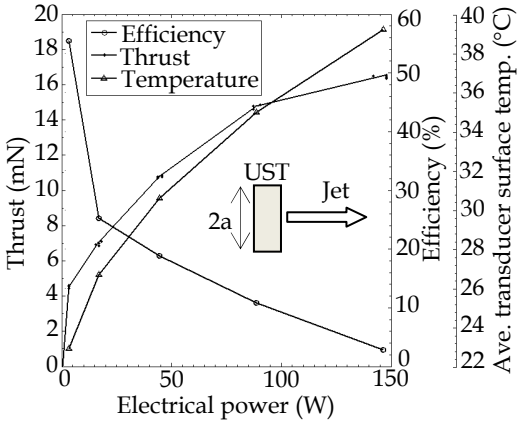

Fig. 19. Thrust force generated, acoustic efficiency, and average surface temperature versus the electrical power driving the UST. Gradients of tangent at each of the clusters of thrust points indicate the UST efficiency. Low power operation generally gives higher efficiency, but at a trivial lower thrust. At high output power, thrust generally saturates.

Next, substitute Eq. (13) into Eq. (14) to determine T_p, which is then substituted into Eq. (11) together with Eq. (12) to determine T_{mid}. With C = [11.26, 11.38, 11.81, 12.53, 13.62]nF and tan $\delta \approx$ 0.4%, the calculated values of T_{mid} are [23.84, 31.12, 42.49, 59.35, 82.59]°C at average output voltage E_{rms} = [12.75, 29, 47.5, 66.5, 85.5]V$_{rms}$. The superfluous heat, Q_l (W), can be calculated using

$$Q_l = \frac{(T_{mid} - T_e)}{R_{eq}} \tag{16}$$

where the equivalent thermal resistance, $R_{eq} = \frac{x_p\left(1/\pi^2 + 1/4\right)}{4k_pA_p} + \frac{x_e}{k_eA_e}$, for the transducer distance from $x = 0$ to the epoxy surface. We plot this heat loss against the amplifier output voltage, E_{rms}, in Fig. 20. Introducing a dimensionless parameter, Q_l/P, which is the ratio of the heat loss energy Eq. (16) to the electrical power supplied Eq. (4), as

$$\frac{Q_l}{P} = \frac{(T_{mid} - T_e)\mathrm{Re}(\Re)}{R_{eq}E_{rms}^2}. \tag{17}$$

We refer to this parameter as the lossy ratio. A large lossy ratio means more electrical energy has been converted to superfluous heat and a small ratio indicates most of the electrical energy has been converted to thrust. This ratio is also plotted in Fig. 20. Note that although the minimum of the graph signifies minimal heat loss to the electrical power supplied, it does not indicate the maximum thrust.

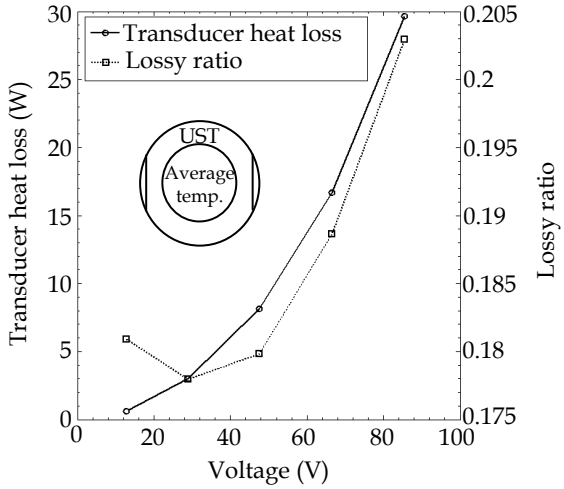

Fig. 20. Superfluous heat loss through the surface of the UST versus output voltage, E_{rms}. An increase in output voltage is generally associated with an increase in heat loss. The minimum of the lossy curve signifies the least heat loss in the system. Higher lossy ratio means more electrical energy is converted into heat losses instead of proportionately thrust.

3.4 Thermal losses design considerations

To determine the maximum thrust without significant loss due to heating, we will consider acoustic efficiency above 10% to be a practical value for this setup. From Fig. 19, the electrical power necessary to generate 10% efficiency would be less than 95W. From (4), and $\Re = 50\Omega$, E_{rms} is found to be $69V_{rms}$. When this voltage is applied across the transducer, from Fig. 19, a UST thrust of about 15mN can be expected. Obviously increasing the voltage will

increase the thrust but not appreciably; instead most added energy will be converted to heat losses, which becomes undesirable in the UST design scheme.

Finally, we verify that T_{mid} is not higher than the Curie temperature of the transducer, specified by the manufacturer at 320°C, to maintain its poled lattice integrity. We also validate the Biot number (Bi), which must be Bi « 1 to justify the temperature within the transducer to be relatively even. From the above parameters, $\mathrm{Bi} = \bar{h}x_e / k_e$ = [0.0682, 0.0655, 0.0600, 0.0491, 0.0382]. More importantly, this condition must also be satisfied for lump-capacity solution in Eq. (15) to be accurate.

4. Conclusion

The ultrasonic thruster technology could bring about interesting and novel attributes to robotic propulsion devices and systems. These include low cost and high robustness when applied at the centimeter scale or smaller. The robustness is due to the fact that the UST effectively has no moving parts, and will not biofoul – these are properties unavailable in the rotary and biomimetic propulsors in use today. Our experiments indicated that frequency, and voltage level can both strongly influence the behavior of the UST, in terms of wake, thrust, and efficiency. We have successfully implemented three sub-centimeter UST devices into a small robot, and made calculations showing short missions can be developed with such craft, despite its inherently low propulsive efficiency.

We have also studied the heating of ultrasonic transducers under conditions of thrust production. In view of practical application of the ultrasonic transducer in the medical field, it has been reported that clinical ultrasonic probes generate considerable heat when driven at off-resonance frequencies (Duck, et al., 1989). Most medical ultrasonic devices have a safety regulation on the level of power that the transducer can produce; for example, the IEC Standard 60606-2-37 limits the surface temperature of ultrasonic transducer to 43°C. In extreme cases, ultrasonic probes could reach a steady-state temperature of 80°C in ambient air at 25°C; obviously this is not suitable for human contact in practice. While the UST is not subject to complying with this standard, a UST device is still limited by extreme heating which may cause physical damage, and also because at high temperature conditions it suffers a saturation in thrust. It may be possible to minimize or harness heat for recycling in the UST system architecture, or even recoup a part of it through specialized nozzle appendages so as to enhance efficiency. For example, the backing layer of the transducer can be ventilated or cooled to remove heat. (Deardorff & Diederich, 2000) demonstrated using a water-cooling system and reported not only it does not reduce the acoustic intensity or beam distribution, but also allows more than 45W additional power supplied to the transducer. Indeed, its thrust assistive quality remains to be investigated.

Clearly UST technology would benefit from further developmental work on application-specific areas. The UST could, for example, complement an existing propulsor system to fine tune maneuvering, or to strategically control or manipulate a flow-field for other purposes. Propulsive efficiency could conceivably be enhanced by developing a waveguide external to the transducer. The use of DPIV for characterizing UST properties is considerably richer than velocity measurement using hot wire method alone, and could also aid new transducer designs traceable to the wake field. New applications, designed to exploit the above UST's

unique attributes, will certainly find this technology a valuable solution. With these insights, the UST could uncover its potential as an enabler for very small crafts, and might find uses in other completely separate applications.

5. Acknowledgment

This research was supported by the Singapore National Research Foundation (NRF) through the Singapore-MIT Alliance for Research and Technology (SMART) Centre, Centre for Environmental Sensing and Modeling (CENSAM). The authors are also grateful to M. Triantafyllou and B. Simpson for access to a DPIV system.

6. References

Allison, E. M., Springer, G. S., & Van Dam, J. (2008). Ultrasonic propulsion. *Journal of Propulsion and Power, 24*(Compendex), 547-553.

Blackstock, D. T. (2000). *Fundamentals of physical acoustics*: New York : Wiley.

Carlton, J. (2007). *Marine propellers and propulsion*: Oxford : Butterworth-Heinemann.

Deardorff, D. L., & Diederich, C. J. (2000). Ultrasound applicators with internal water-cooling for high-powered interstitial thermal therapy. *IEEE Transactions on Biomedical Engineering, 47*(Compendex), 1356-1365.

Doty, K. L., Arroyo, A. A., Crane, C., Jantz, S., Novick, D., Pitzer, R., et al. (1998). *An autonomous micro-submarine swarm and miniature submarine delivery system concept.* Paper presented at the Florida Conference on Recent Advances in Robotics, Florida.

Duck, F. A., Starritt, H. C., ter Haar, G. R., & Lunt, M. J. (1989). Surface heating of diagnostic ultrasound transducers. *British Journal of Radiology, 62*(Copyright 1990, IEE), 1005-1013.

Egeskov, P., Bech, M., Bowley, R., & Aage, C. (1995). *Pipeline inspection using an autonomous underwater vehicle.* Paper presented at the Proceedings of the 14th International Conference on Offshore Mechanics and Arctic Engineering. Part 5 (of 5), June 18, 1995 - June 22, 1995, Copenhagen, Den.

Hariharan, P., Myers, M. R., Robinson, R. A., Maruvada, S. H., Sliwa, J., & Banerjee, R. K. (2008). Characterization of high intensity focused ultrasound transducers using acoustic streaming. *Journal of the Acoustical Society of America, 123*(Compendex), 1706-1719.

Hoerner, S. F. (1965). *Fluid-dynamic drag: practical information on aerodynamic drag and hydrodynamic resistance*: Midland Park, N. J.

Kamakura, T., Sudo, T., Matsuda, K., & Kumamoto, Y. (1996). Time evolution of acoustic streaming from a planar ultrasound source. *Journal of the Acoustical Society of America, 100*(Compendex), 132-132.

Lewis, G. K., & Olbricht, W. L. (2008). Development of a portable therapeutic and high intensity ultrasound system for military, medical, and research use. *Review of Scientific Instruments, 79*(Compendex).

Lienhard IV, J. H., & Lienhard V, J. H. (2002). *A heat transfer textbook* Cambridge, Mass. : Phlogiston Press.

Lighthill, J. (1978). Acoustic streaming. *Journal of Sound and Vibration, 61*(Copyright 1979, IEE), 391-418.

Loh, B.-G., & Lee, D.-R. (2004). Heat transfer characteristics of acoustic streaming by longitudinal ultrasonic vibration. *Journal of Thermophysics and Heat Transfer, 18*(Compendex), 94-99.

Myers, M. R., Hariharan, P., & Banerjee, R. K. (2008). Direct methods for characterizing high-intensity focused ultrasound transducers using acoustic streaming. *Journal of the Acoustical Society of America, 124*(Compendex), 1790-1802.

Nobunaga, S. (2004). European Patent Office: H. Electronic.

Panchal, C. B., Takahashi, P. K., & Avery, W. (1995). Biofouling control using ultrasonic and ultraviolet treatments (pp. 13): Department of Energy, Office of Scientific and Technical Information (DOE-OSTI).

Rudenko, O. V., & Soluian, S. I. (1977). Theoretical foundations of nonlinear acoustics. 274.

Sfakiotakis, M., Lane, D. M., & Davies, J. B. C. (1999). Review of fish swimming modes for aquatic locomotion. *IEEE Journal of Oceanic Engineering, 24*(Compendex), 237-252.

Sherrit, S., Bao, X., Sigel, D. A., Gradziel, M. J., Askins, S. A., Dolgin, B. P., et al. (2001). *Characterization of transducers and resonators under high drive levels.* Paper presented at the 2001 IEEE Ultrasonics Symposium. Proceedings. An International Symposium, 7-10 Oct. 2001, Piscataway, NJ, USA.

Tan, A. C. H., & Hover, F. S. (2009). *Correlating the ultrasonic thrust force with acoustic streaming velocity.* Paper presented at the 2009 IEEE International Ultrasonics Symposium, 20-23 Sept. 2009, Piscataway, NJ, USA.

Tan, A. C. H., & Hover, F. S. (2010a). *On the influence of transducer heating in underwater ultrasonic thrusters.* Paper presented at the the 20th International Congress on Acoustics Sydney, Australia.

Tan, A. C. H., & Hover, F. S. (2010b). *Thrust and wake characterization in small, robust ultrasonic thrusters.* Paper presented at the 2010 OCEANS MTS/IEEE SEATTLE, 20-23 Sept. 2010, Piscataway, NJ, USA.

Tan, A. C. H., & Tanaka, N. (2006). *The safety issues of intense airborne ultrasound: Parametric array loudspeaker.* Paper presented at the Proceedings of the 13th International Congress on Sound and Vibration, Vienna, Austria.

Trimmer, W., & Jebens, R. (1989). *Actuators for micro robots.* Paper presented at the Proceedings. 1989 IEEE International Conference on Robotics and Automation (Cat. No.89CH2750-8), 14-19 May 1989, Washington, DC, USA.

Wang, Z., Zhu, J., Qiu, X., Tang, R., Yu, C., Oiler, J., et al. (2011). *Directional acoustic underwater thruster.* Paper presented at the 2011 IEEE 24th International Conference on Micro Electro Mechanical Systems (MEMS 2011), 23-27 Jan. 2011, Piscataway, NJ, USA.

Yu, H., & Kim, E. S. (2004). *Ultrasonic underwater thruster.* Paper presented at the 17th IEEE International Conference on Micro Electro Mechanical Systems (MEMS): Maastricht MEMS 2004 Technical Digest, January 25, 2004 - January 29, 2004, Maastricht, Netherlands.

Zhou, S.-W., & Rogers, C. A. (1995). Heat generation, temperature, and thermal stress of structurally integrated piezo-actuators. *Journal of Intelligent Material Systems and Structures, 6*(Compendex), 372-379.

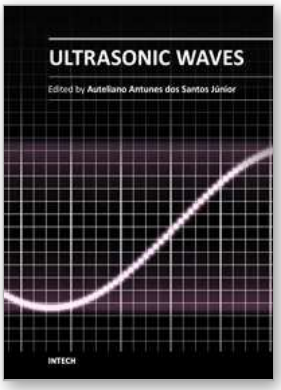

Ultrasonic Waves
Edited by Dr Santos

ISBN 978-953-51-0201-4
Hard cover, 282 pages
Publisher InTech
Published online 07, March, 2012
Published in print edition March, 2012

Ultrasonic waves are well-known for their broad range of applications. They can be employed in various fields of knowledge such as medicine, engineering, physics, biology, materials etc. A characteristic presented in all applications is the simplicity of the instrumentation involved, even knowing that the methods are mostly very complex, sometimes requiring analytical and numerical developments. This book presents a number of state-of-the-art applications of ultrasonic waves, developed by the main researchers in their scientific fields from all around the world. Phased array modelling, ultrasonic thrusters, positioning systems, tomography, projection, gas hydrate bearing sediments and Doppler Velocimetry are some of the topics discussed, which, together with materials characterization, mining, corrosion, and gas removal by ultrasonic techniques, form an exciting set of updated knowledge. Theoretical advances on ultrasonic waves analysis are presented in every chapter, especially in those about modelling the generation and propagation of waves, and the influence of Goldberg's number on approximation for finite amplitude acoustic waves. Readers will find this book ta valuable source of information where authors describe their works in a clear way, basing them on relevant bibliographic references and actual challenges of their field of study.

InTech Europe
University Campus STeP Ri
Slavka Krautzeka 83/A
51000 Rijeka, Croatia
Phone: +385 (51) 770 447
Fax: +385 (51) 686 166
www.intechopen.com

InTech China
Unit 405, Office Block, Hotel Equatorial Shanghai
No.65, Yan An Road (West), Shanghai, 200040, China
中国上海市延安西路65号上海国际贵都大饭店办公楼405单元
Phone: +86-21-62489820
Fax: +86-21-62489821